ADVANCED OPTICAL MATERIALS
www.advopticalmat.de

Holistic Nanowire Laser Characterization as a Route to Optimal Design

Stephen A Church, Nikesh Patel, Ruqaiya Al-Abri, Nawal Al-Amairi, Yunyan Zhang, Huiyun Liu, and Patrick Parkinson**

Nanowire lasers are sought for near-field and on-chip photonic applications as they provide integrable, coherent, and monochromatic radiation: the functional performance (threshold and wavelength) is dependent on both the opto-electronic and crystallographic properties of each nanowire. However, scalable bottom-up manufacturing techniques often suffer from inter-nanowire variation, leading to differences in yield and performance between individual nanowires. Establishing the relationship between manufacturing controls, geometric and material properties, and the lasing performance is a crucial step toward optimisation; however, this is challenging to achieve due to the interdependance of such properties. Here, a high-throughput correlative approach is presented to characterise over 5000 individual GaAsP/GaAs multiple quantum well nanowire lasers. Fitting the spontaneous emission provides the threshold carrier density, while coherence length measurements determine the end-facet reflectivity. The performance is intrinsically related to the width of a single quantum well due to quantum confinement and bandfilling effects. Unexpectedly, there is no strong relationship between the properties of the lasing cavity and the threshold: instead the threshold is negatively correlated with the non-radiative recombination lifetime of the carriers. This approach therefore provides an optimisation strategy that is not accessible through small-scale studies.

1. Introduction

Semiconductor nanowires (NWs) can be designed to act as both a gain medium and a Fabry-Pérot cavity, due to the high reflectivity of their end-facets,[1] facilitating room temperature lasing with appropriate optical pumping.[2] These structures can provide monochromatic and coherent light sources for photonic circuits[2] and sensing applications[3] and can advantageously be grown directly on silicon substrates[4] and waveguides.[5]

The performance of NW lasers (NWLs) can be characterised by the lasing threshold and the optical modal structure, which must be optimized to the specific application. The NWL platform is compatible with a wide variety of material systems and is therefore adaptable: by selecting the appropriate gain medium material, lasing wavelengths ranging from the ultra-violet (ZnO,[6] GaN[7,8]) to the visible (CdS,[9] perovskites[10]) and the infra-red (GaAs,[11] InP,[12] CdSe[13]) have been demonstrated. Further control of the lasing wavelength can be achieved by changing the material composition,[10] or by incorporating a heterostructure.[14] Careful design of these can also reduce the lasing threshold by increasing the spatial overlap between the gain medium and the lasing mode.[15] However, variation in one or more of the properties such as the NW size, material quality or cavity can lead to significant changes in their performance.[16] It is therefore essential to develop an experimental understanding of how each of these parameters impact the performance to facilitate future fabrication improvements.

The lasing cavity is expected to determine the modal structure of the lasing emission.[8] For Fabry-Perot cavities, this is defined by the end facets of the NW so that the NW length determines the longitudinal modes which can lase.[17] Mode confinement must also be considered, which is influenced by the NW width, the lasing wavelength, the lasing mode and the refractive index difference between the NW and the surroundings.[18]

The reflectivity of the end facets impacts both the degree of optical feedback in the laser and the output coupling. For in-plane NWLs the native reflectivity of the end facets is enhanced

S. A. Church, N. Patel, R. Al-Abri, N. Al-Amairi, P. Parkinson
Department of Physics and Astronomy and Photon Science Institute
the University of Manchester
Manchester M13 9PL, UK
E-mail: stephen.church@manchester.ac.uk;
patrick.parkinson@manchester.ac.uk
Y. Zhang
School of Micro-Nano Electronics
Zhejiang University
Zhejiang, Hangzhou 311200, China
H. Liu
Department of Electronic and Electrical Engineering
UCL, Malet Place
London, WC1E 7JE, UK
The ORCID identification number(s) for the author(s) of this article can be found under https://doi.org/10.1002/adom.202202476.

DOI: 10.1002/adom.202202476

above the Fresnel reflection coefficients[1] and is often sufficient for lasing.[19] This can be further enhanced using reflective layers designed for the lasing wavelength.[20] This reflectivity is strongly coupled to the mode confinement in the NW, and theoretical studies have shown that these relationships can be complex.[1] This is because optical far-field approximations are not valid when considering the behaviours of a sub-wavelength cavity - and as a result these effects are challenging to investigate experimentally.

For both vapor-liquid solid (VLS) and selective area growth (SAE) NWs there is an additional complication: since the growth is driven by thermodynamic processes, the NWs demonstrate variation in material and cavity properties that influence the lasing performance.[21] It is therefore difficult to vary a single property in isolation, which makes any systematic study of these effects a challenge.

We utilise advancements in laboratory automation to explore the complex, multidimensional parameter space created by inter-NW heterogeneity.[22] This methodology individually characterises the gain and cavity properties of thousands of NWLs using a suite of optical characterisation techniques. This includes power-dependent photoluminescence spectroscopy, to assess the lasing wavelength and thresholds, time-correlated single photon counting, to determine the carrier lifetimes, waveguiding studies to investigate distributed losses[23] and interferometry to determine the laser coherence length and end-facet reflectivities.[24] Correlating the results from these independent measurements provides unique insights into the lasing properties of NWs that would otherwise be inaccessible.

We have applied this approach to 5195 GaAs/GaAsP NWLs that have three, highly-strained quantum wells (QWs) in a core-shell structure, and threshold fluences as low as 6 μJ cm^{-2} at room temperature.[24,25] We correlate the properties of the cavity and gain medium to the threshold carrier density in the QWs and demonstrate that it is the properties of the QWs that limit the NWL performance. The approach is modular and scalable by design, and therefore suitable for characterisation of other NWL material systems, whilst being widely applicable to emerging opto-electronic materials.

2. Results and Discussion

For NWLs, the lasing threshold gain is driven by the interplay between gain and loss mechanisms in the Fabry-Pérot cavity. The amount of gain is proposed to be determined by both the design and material quality of the active region.[26] The losses, on the other hand, will likely be affected by the properties of the lasing cavity,[16] which is predominantly determined by the reflectivity of the end facets,[1] along with distributed losses that may be driven by reabsorption of lasing radiation[27] and waveguide losses.

However, the magnitude of these relationships has not been established. To investigate the factors that limit the lasing performance of the NWs, it is necessary to characterise all of these gain and cavity properties of each NW. Specifically, we use this to identify the strength of the correlation between performance and cavity parameters, and performance and material parameters: this can be used to determine an optimisation strategy. This approach was initially applied to single NWs, before being scaled up to a large number of individual NWs to understand how these different properties influence each other.

2.1. Single Nanowire Results

A population of 5195 GaAs/GaAsP multiple QW NWs, grown using a previously described recipe,[24] were removed from their growth substrate into solution and drop-cast onto a Si substrate to study their optical properties.

A dark field optical microscopy image was recorded for each NW, an example for a specific NW (labelled A) is shown in **Figure 1**a: image analysis was performed to determine the width and length of each NW. The measured NW width was limited by the resolution of the microscope; therefore supplementary scanning electron microscopy (SEM) was also performed, providing a higher-resolution image, also shown in Figure 1a: SEM and optical images were matched for a subset of 2492 NWs. The mean NW width, and standard deviation (SD), was (0.77 ± 0.25) μm and the mean length was (16 ± 4) μm. Further details of the image comparison and statistics are given in the Supporting Information.

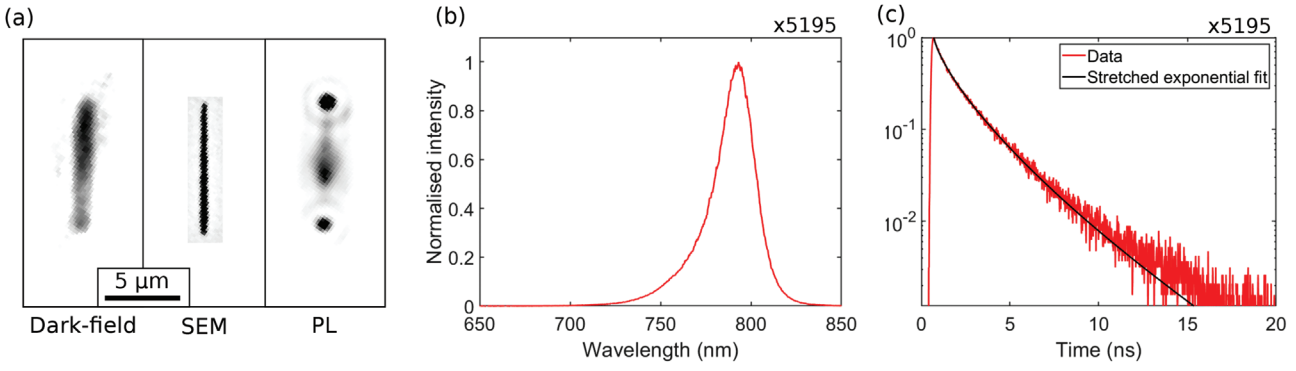

Figure 1. Imaging and spectroscopic characterisation for NW A. The numbers (x—-) provide the number of NWs that a successful experiment and analysis was performed. a) A dark-field optical image, SEM image and photoluminescence (PL)-emission image of the same NW. b) A PL spectrum, recorded under low power excitation with a continuous wave (CW) laser. c) A PL time decay, also measured with a low fluence: this has been fit with a stretched exponential decay, defined in Equation (7).

Low fluence photoluminescence (PL) spectroscopy was performed by exciting each NW using a frequency-doubled diode-pumped solid state continuous wave 532 nm laser, focused to a spot diameter of 3 µm with a power of 0.5 mV at the sample. The spatial emission profile of the NW was measuring using imaging (Figure 1a), and the PL spectrum was also measured: an example spectrum for NW A is shown in Figure 1b. Under these low-power excitation conditions the spectral shape is independent of the excitation power density. There is also minimal axial spectral variation along the NW. Therefore, for below-threshold studies on these NWs, this spectral measurement at a single point provides a result that is both reproducible and representative of the entire NW.

Time correlated single-photon counting measurements (TCSPC) were performed far below lasing threshold using 633 nm, 200 fs excitation pulses from an optical parametric amplifier system, that were attenuated and defocussed at the sample position to achieve an excitation fluence of approximately 15 µJ cm^{-2} across a uniform spot of 63 µm diameter. An example of the resultant PL time decay on NW A is shown in Figure 1c. The recombination lifetime was was fit by a stretched exponential model defined by Equation (7), with a power factor of 0.71: this suggests that there is a degree of disorder in the QWs.[28] The lifetime was 1.0 ns for this NW. Under these conditions, both radiative and non-radiative Shockley-Reed-Hall (SRH) recombination are likely to contribute to these dynamics, which is explored further in the Supporting Information. An estimated internal quantum efficiency (IQE) of 39 % was determined using this approach. Further analysis of the IQE and the power factor is provided in the Supporting Information.

The lasing properties of each NW were characterised by recording the emission spectrum at different excitation fluences. For these experiments, the same pulsed laser system was used to achieved a uniform spot of (73 ± 1) µm diameter with fluences up to 2000 µJ cm^{-2}. Critically, this wavelength avoids exciting the direct bandgap of the QW barriers,[24] and so avoids excessive heating from carrier cooling and complications due to carrier capture from the barriers. An example of these spectra for a second wire, NW B. is shown in **Figure 2**a, which shows spectra for fluences between 19 µJ/cm^2/pulse and 270 µJ/cm^2/pulse. At low excitation fluences, only the broad spontaneous PL emission can be observed. As the fluence is increased above a threshold, a sharp lasing emission peak with a full-width-half-maximum (FWHM) of approximately 1.5 nm appears in the spectrum.

Analysis of power-dependent photoluminescence spectrum provides the primary lasing wavelength, the threshold and the inter-modal spacing. For NWLs where longitudinal mode

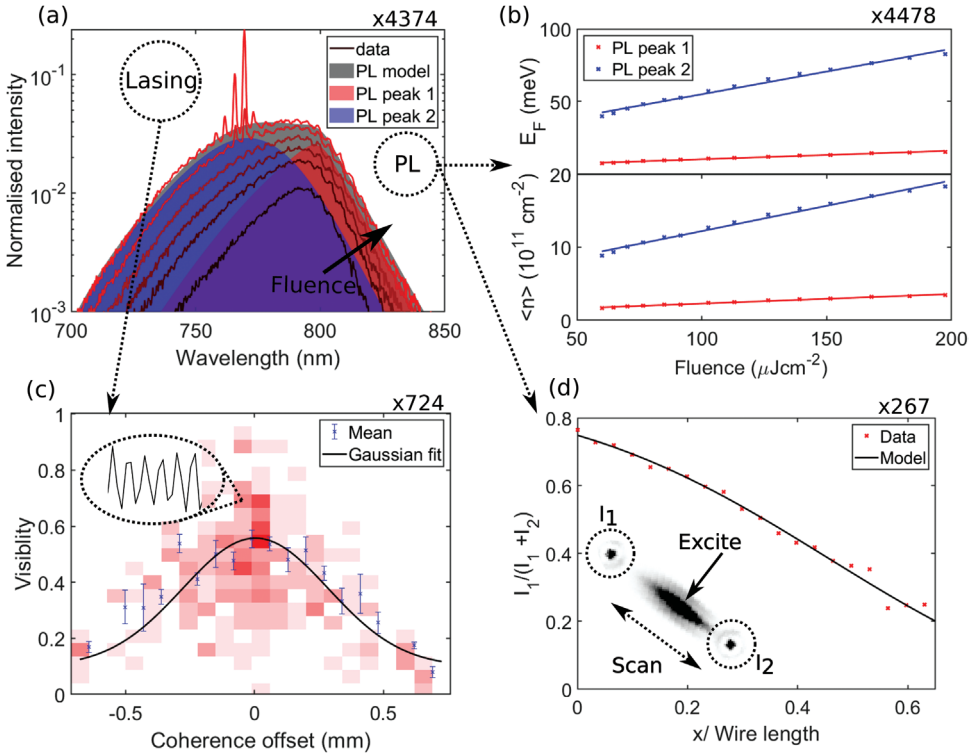

Figure 2. Characterisation of the lasing properties for NW B. The numbers (x—-) provide the number of NWs that a successful experiment and analysis was performed. a) Emission spectra showing PL and lasing emission with excitation fluence varying from 19 µJ per cm^2 per pulse to 270 µJ per cm^2 per pulse. An LSW fit is shown applied to the highest fluence PL spectrum, demonstrating the contribution from two PL peaks. b) The variation of Fermi energy and carrier density with excitation fluence in two different QWs, extracted from Lasher-Stern-Wurfel fits to the PL spectra. A linear fit to the data has been shown. c) A 2D histogram showing how the visibility of the interference fringes changes with distance from the zero path length position. The median and SD values for each horizontal bin are given in blue as a guide for the eye. A Gaussian fit has been applied to the visibility data, to extract the coherence length. Inset is a section of the raw interferogram, showing the interference fringes. d) A plot of the intensity of light coupling out of the NW end-facets versus position of the excitation spot. This has been fit with a model, defined by Equation (2), to extract a value for the distributed losses.

structure is expected to dominate, this can be further used to determined the effective cavity length. An example of the threshold and length analysis is provided in the Supporting Information. For NW B, the threshold is 230 μJ/cm^2/pulse and the wavelength is 773 nm, and this approach was successfully applied to 4460 (84 %) of the NWs. The other NWs could not be analysed automatically due to the emergence of multiple peaks. An additional filtering step was applied to these results to ensure that only threshold values with a low uncertainty were considered for correlation studies. This excluded an additional 2% of wires from further analysis, and a similar approach was applied for the other aspects of this study.

The spectra in Figure 2a also contain a broad photoluminescence emission band, which contains two emission peaks, peak 1 at longer wavelengths, and peak 2 at shorter wavelengths. These peaks were fit using a Lasher-Stern-Wurfel (LSW) model,[29] for two-dimensional states defined by Equation (5) in the experimental section. The PL transition energy, and σ, which is a measure of the symmetrical disorder in the QW,[27] were extracted from the fitting results. The Urbach energy is another fitting parameter, that is discussed in the Supporting Information. For NW B, this yielded transition energies of 1.551 eV and 1.591 eV. σ was found to be 15 meV and 14 meV for these peaks, indicating a similar degree of disorder in both peaks. We attribute peak 1 to carrier recombination in a QW, and we consider several candidates for peak 2.

Firstly, peak 2 may originate from carrier recombination in different QWs in the core-shell structure. This is supported by considering the band structure of the three QWs in the NW. Due to the close proximity to the NW core, which has a different alloy composition, the inner-most QW has an asymmetrical barrier.[24] One-dimensional numerical solutions of the Schrödinger Equation (SE), shown in the Supporting Information, demonstrate that this effect can increase the E_{11} ground state transition energy by 15 meV when compared with the other QWs.

As an alternative explanation, the shorter wavelength recombination peak may be a product of bandfilling effects in the same QW at high fluences. This could result in carrier recombination through the E_{22} transition in the same QW. Using the SE solutions, this results in a transition energy that is up to 350 meV higher than the ground state, for realistic QW widths. Alternatively, carriers could be overflowing from the QW into the indirect X state in the QW barriers, which results in a transition energy of 1.98 eV.[24] These transition energies are both significantly larger than those observed in the PL spectra.

The bandfilling effects in these QWs are directly linked to the FWHM of the emission. A global LSW fit was applied to the full set of fluence-dependent PL spectra in Figure 2a: properties such as the bandgap and σ were kept constant with fluence, whilst allowing the Fermi energy and peak amplitude to vary. To minimise the total number of fitting parameters, it was assumed that the Fermi energy and amplitude of each peak were related by a constant factor that was independent of fluence. The Fermi energy at each excitation fluence for NW B is shown in Figure 2b. As this experiment used pulsed excitation, this is the time-averaged E_F, or $\langle E_F \rangle$, which is weighted by the instantaneous intensity of the PL, $I_{PL}(t)$ and is hence skewed toward early times. This is described by:

$$\langle E_F \rangle = \frac{E_F(t) \times I_{PL}(t)}{\int_0^{5\mu s} I_{PL}(t)\, dt} \quad (1)$$

integrating over the laser repetition rate of 5 μs. At fluences below 50 μJ cm^{-2} the Fermi energy cannot be extracted reliably, due to large fitting errors. However, above 50 μJ cm^{-2}, and at threshold, a linear correlation is observed between excitation fluence and Fermi energy. This suggests that we only observe emission from E_{11} transitions in the QWs. The linear fit does not pass through the origin, and so E_F must vary superlinearly at low fluences. This is suggestive of a reduced density of states at low energy due to the impact of disorder on the bandstructure.

A suitable fit was achieved whilst maintaining a constant relative amplitude of the two PL peaks. Therefore, in this fluence regime, there is no significant change in the relative occupation of the states associated with each peak and there is no significant carrier transfer between the states. As a result, it is unlikely that peak 2 originates either from the E_{22} transition or from the QW barrier states. We therefore attribute peak 2 to the E_{11} transition in the QW closest to the NW core (QW-core), which has a higher transition energy than the other QWs (QW-shell). The zero strain equivalent (ZSE) widths of these QWs were estimated using one dimensional numerical solutions of the SE, and are given in **Figure 3**b. These calculations do not consider the impact of higher order effects, such as strain in the QW, more details of which are provided in the Supporting Information. Strain is likely to have an impact on the band alignment in the QWs, and therefore the transition energies, but, crucially, the variation of transition energies will remain comparable for small-magnitude strains. Therefore, any variation in the QW width will have a similar effect on the ZSE width. This approach gave a ZSE width of 3.8 nm for the QW-core and 4.6 nm for the QW-shell.

Our model provides a route to study each emission in isolation: As shown in Figure 2a, the emission from the QW-core (peak 2) has a larger FWHM than the QW-shell (peak 1). The LSW model therefore calculates a larger Fermi energy: Figure 2b shows that that the Fermi energy in the QW-core is around double that of the QW-shell. This is the result of a higher carrier density in the core-QW. COMSOL simulations in the Supporting Information suggest that the absorption of photons in each QW is expected to be guided by the spatial overlap of the QWs with the electric fields of the excitation.

It is typical for lasing thresholds to be reported in units of fluence (μJ cm^{-2}).[19,30] However, using this approach, it is difficult to compare results from different NWs due to variation in experimental conditions. For example, the threshold fluence can be highly dependent on the excitation wavelength.[24] It is also expected that substrates with different refractive indices will modify the threshold by changing the cavity properties.[26] Additionally, differences in absorption and carrier dynamics may also cause changes in the threshold: this effect is explored by finite difference time domain simulations in the Supporting Information. To remove the resultant ambiguity, it is necessary to move to a more direct measurement of the laser threshold. This can be achieved by considering the threshold areal carrier density within the QWs.

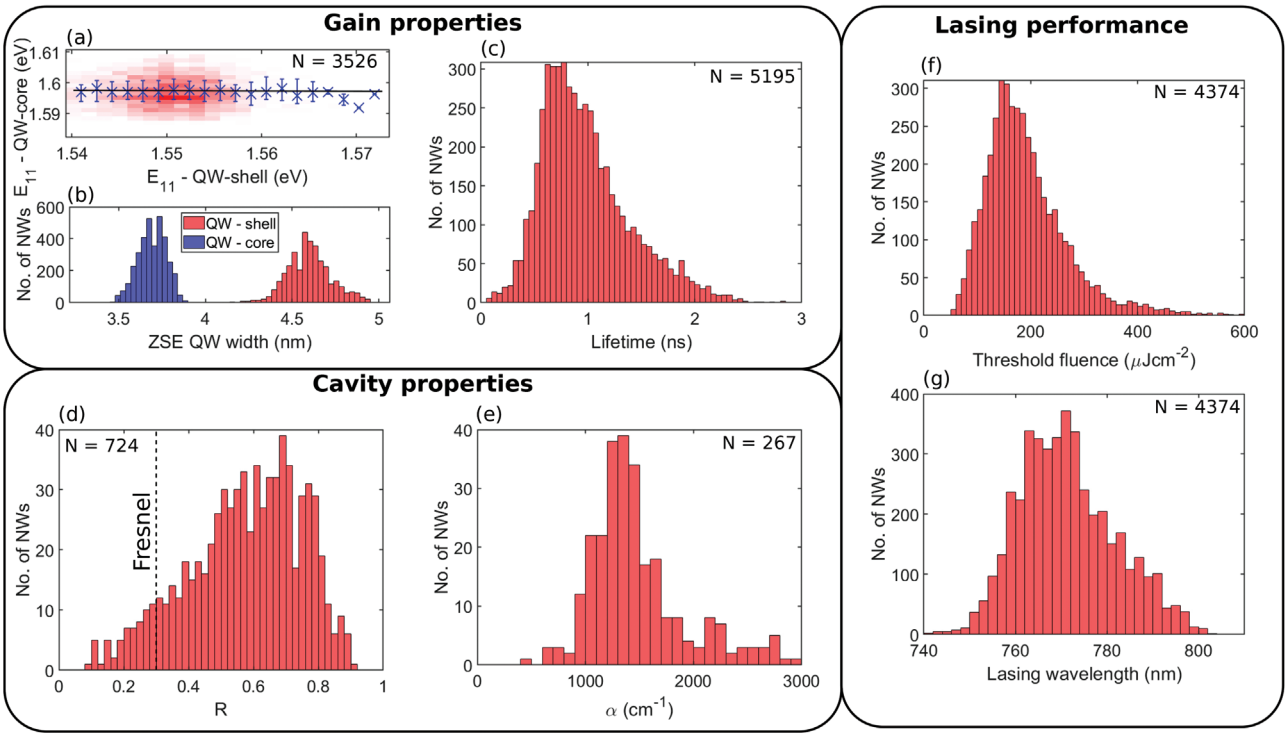

Figure 3. Distributions of the parameters describing the gain medium, cavity properties and lasing performance, across the NW population. a) A 2D histogram showing the lack of correlation between the E_{11} transition energies of each QW. The blue crossed and error bars are the median and the inter-quartile range values for each bin. b) The estimated ZSE width of two QWs in the core/shell structure, (4.6 ± 0.1) nm and (3.7 ± 0.1) nm. c) The carrier recombination lifetime (0.9 ± 0.4) ns. d) The cavity reflectivity (0.6 ± 0.2). e) The distributed losses (1400 ± 400) cm^{-1}. f) The threshold fluence (180 ± 80) μJ/cm^2/pulse. g) The initial lasing wavelength (770 ± 10) nm.

Our bandfilling analysis provides a route to determine the averaged carrier density as it is related to the Fermi energy. Using Equation (6), defined in Section 4, the time-averaged carrier density in the QWs, $\langle n \rangle$, was calculated. To convert this to the initial carrier density, n_0, the PL time decays were also measured close to the lasing threshold (at 0.6 P_{th}) under the same excitation conditions. For NW B, this provided a threshold n_0 of 3.9×10^{15} carriers per cm^2 for the QW-core. This analysis is discussed in detail in Section 4, and lifetime statistics are shown in the Supporting Information.

The intensity reflectivities of the end-facets of the NW were determined using an interferometric approach based on ref. [24]. The interferogram of the lasing emission above threshold was measured and the fringe visibility was calculated by measuring the peak-to-peak amplitude across the interferogram, using Equation (9): Figure 2c shows how the fringe visibility varies with distance around the zero path-length position. The scatter around the fitted Gaussian is symmetrical in nature, and originates from random error in the sampling position of each point in the interferogram, which is a consequence of the fast stage speeds required for high-throughput measurement. The FWHM of the Gaussian is equal to the coherence length of the emission, which is 0.7 mm for NW B. This coherence length is much larger than the NW length (20 μm), and corresponds to a lasing Q factor of 900.

Using Equation (10) in Section 4, the coherence length was used to calculate the intensity reflectivity of the cavity, described as the geometric mean of the end-facet reflectivity. This had a value of 0.56 for NW B. This reflectivity is larger than the far-field reflectivity calculated using the Fresnel reflection coefficients (0.30), as expected from theoretical calculations.[1] Fluorescence imaging was used to determine the reflectivity of each facet separately: this analysis is shown in the Supporting Information. The reflectivity measurements were performed for 1737 NWs, successfully finding the reflectivity of 724 NWs. The roughly 60% failure rate in our analysis was due to a relatively low collected intensity of laser radiation from each NW, which resulted in large uncertainties in the coherence length and reflectivity values.

The distributed losses in the lasing cavity were estimated by imaging the NW emission when exciting with a 2 μm-diameter spot from a 0.5 mW HeNe laser. The NW orientation angle was determined through automatic analysis of the images: this enabled, as depicted in the inset of Figure 2d, the excitation spot to be automatically scanned along the NW length and the emission intensity at the end facets to be recorded. This scanning approach can be scaled up to study hundreds of individual NWs without the need for further human input. The change in intensity of light emission from each end-facet was measured to produce the data shown in Figure 2d. The intensity of emission from a facet drops approximately exponentially with distance between the excitation point and the facet. Using the Beer–Lambert Law, the distributed losses, α, were found from the ratio of the integrated intensity from each facet, $I_{1,2}$. This is given by Equation (2):

$$\frac{I_1}{I_1+I_2} = A + \left(1 + B\left(\frac{1-R_2}{1-R_1}\right)\frac{\exp(-\alpha(L-x))}{\exp(-\alpha x)}\right)^{-1} \quad (2)$$

where $R_{1,2}$ is the reflectivity of each end facet, x is the distance from facet 1, A is a term accounting for a background baseline in the measurement and B accounts for additional losses. α was (1300 ± 100) cm^{-1} for NW B. The losses were measured for a subset of 267 NWs and they may be due to scattering or coupling from the cavity side-wall, or reabsorption.[27]

2.2. Population Studies

To decouple the impact of lasing cavity and material gain from the threshold, the above investigations were repeated on a large number of individual NWs. As a result, distributions for the previously determined parameters were obtained, which demonstrate the variation across the sample population. These results are summarised by the histograms in Figure 3.

Analysis of the PL spectra extracted the transition energies associated with each PL emission peak for 3526 NWs (Figure 3a), which demonstrates that there is no correlation between these transition energies. This observation, that could not be made from a single-NW measurement, provides further evidence that the shorter wavelength peak does not originate from a QW that is independent from the longer wavelength peak QW.

Additional measurements determined the lifetimes of 5195 NWs (Figure 3c), interferometry was used to find the reflectivity for 724 NWs (Figure 3d), the distributed losses were characterised for 267 NWs ((Figure 3e) and the fluence dependence study found the lasing thresholds and wavelengths for 4374 NWs (Figure 3f,g). The "best in class" NW had a threshold fluence of 51 μJ per cm^2 per pulse at a wavelength of 793 nm.

There is variation in all of the reported parameters, but this is of particular note for the intensity reflectivity, which varies between 0.1 and 0.9. This variation is significantly larger than the uncertainty in parameters that are assumed to be constant, such as the refractive index (which has a 15% uncertainty, see the Supporting Information for more information). Furthermore, the reflectivity does not correlate with any other cavity or gain parameters, and so the variation is likely to be caused by other factors. This could either be related to variation in roughness and faceting of the end of the NW that is broken during the process of transferring the NW from their native substrate,[31] or due to irregular morphology at the NW tip, due to an increase in defects.[32] It has been suggested that deviation from the ideal planar morphology could reduce the reflectivity by up to a factor of 5,[15] which may account for the majority of the observed variation.

The reflectivity of 91% of the NWs is larger than the Fresnel coefficient. This result is compatible with early simulations by Maslov and Ning,[1] who demonstrated that, in the regime of strong waveguiding, the intensity reflectivity of the end facets can be up to three times higher than an infinite planar surface.

The distributions represent a coupled, multidimensional dataset of the NW population. This was analysed using a multiple linear regression model, considering the impact of changes in the lasing cavity and gain medium on the lasing threshold and wavelength. The model parameters are summarised in **Table 1**, and will be discussed further in this section.

Table 1. Outputs from multiple linear regression models that quantify the relative impact of varying NW properties on three different performance metrics.

		Lasing wavelength		Threshold carrier density	
	Variable	Variation (%)	*p*-value	Variation (%)	*p*-value
Gain	Lifetime	–4	0.50	**–36**	**≈0**
	σ	–11	0.11	**–18**	**≈0**
	QW-shell ZSE width	–1	0.95	–3	0.69
	QW-core ZSE width	**48**	**≈0**	**–26**	**≈0**
Cavity	NW width	3	0.61	3	0.52
	NW length	0	0.90	**–13**	**≈0**
	α	–10	0.47	–14	0.19
	Reflectivity	0	0.85	–3	0.21

The variation of the performance metric with each variable is provided as a percentage of the maximum observed variation, and the p-value for each variable is also shown. Variables with a significance within the 3σ (p = 0.003) limit are highlighted in bold.

First, the lasing performance metrics are strongly coupled together. This is demonstrated in **Figure 4**a for the lasing wavelength and threshold carrier density, where an order of magnitude increase in the threshold causes a blueshift of the median lasing wavelength by approximately 10 nm. Reabsorption of emitted light can be invoked to explain such behaviour,[19] however the performance of NWs in these previous reports was dominated by reabsorption in the NW core. For the GaAs/GaAsP NWs studied in this paper, the core has a larger bandgap than the QWs and so reabsorption should be reduced, and therefore the observed variation may have a different origin.

As demonstrated in Figure 4a, the median Fermi energy also varies between 20 meV and 80 meV. This results in a smaller shift in the peak PL wavelength. This shift is due to an increased degree of bandfilling at higher carrier densities. The median lasing wavelength lies between the bandgap and the Fermi level, and the trend in lasing wavelength matches well with the variation in peak PL wavelength. This suggests that the correlation between lasing wavelength and threshold is a signature of bandfilling effects in the QW. The lasing wavelength is consistently redshifted by 2 nm relative to the PL peak, which suggests that there may be an increased modal overlap with the QWs for longer wavelengths.

The effect of the gain medium is determined by looking at the impact of the QW properties. Table 1 shows that the carrier recombination lifetime in the QWs has no relationship with the lasing wavelength, there is however a strong negative correlation with lasing threshold, which is illustrated in Figure 4b. The measured lifetimes vary between approximately 0.5 ns and 2.5 ns. We find that under these conditions, non-radiative recombination has a significant impact on the recombination rate (see the Supporting Information for details). A decrease in the non-radiative rate causes a reduction in the threshold. The non-radiative rate is strongly influenced by defects in the QWs or barriers layers;[32,33] therefore, a higher quality gain medium,

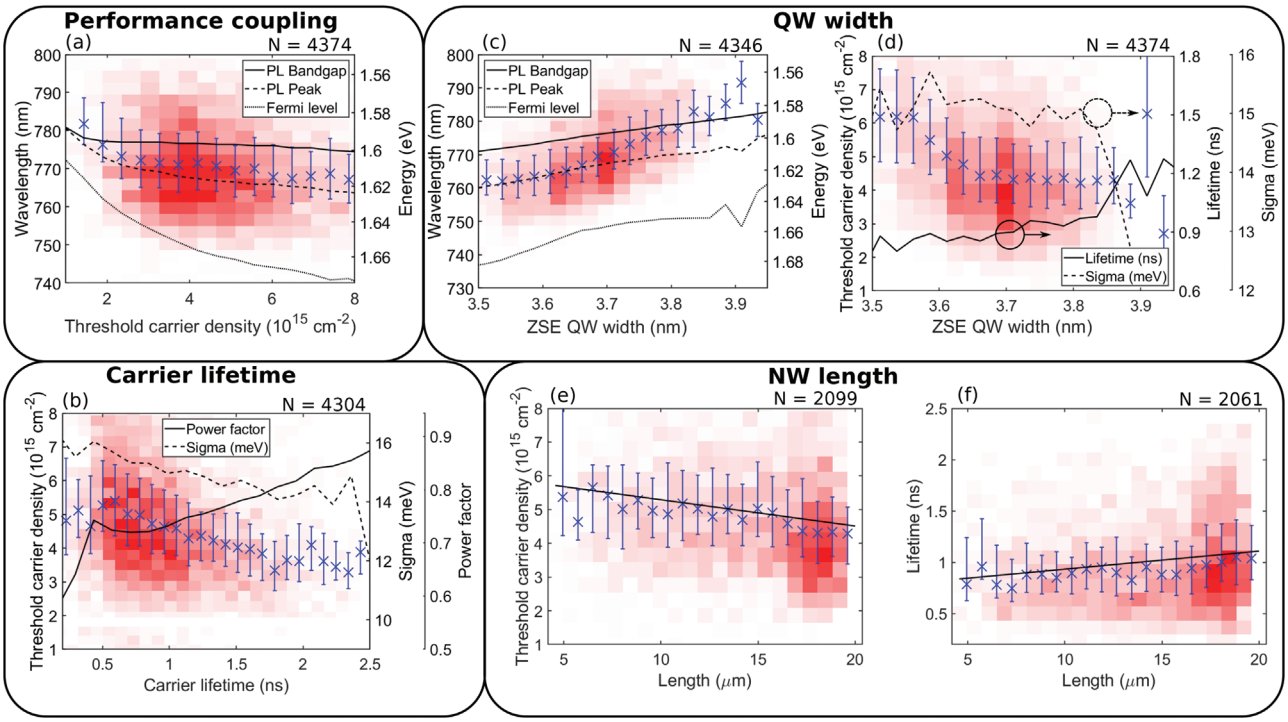

Figure 4. Correlations between different parameters observed across the population. Each plot contains data from the NWs where successful fitting of the independent measurements has been performed: data-points represent median values in each horizontal bin, with the error bars indicating the inter-quartile range. a) Lasing wavelength vs threshold carrier density for 4374 NWs. The plot also includes the median wavelengths corresponding to the PL bandgap, the peak in the LSW PL spectrum and the Fermi level. b) Threshold carrier density vs carrier lifetime for 4304 NWs, a linear fit through the data is shown as a guide to the eye. The plot also includes the median σ, determined from the PL fitting, and the median power factor, taken from the stretched exponential fits to the PL decays at low fluence. c) Lasing wavelength vs QW ZSE width for 4346 NWs. The plot also includes the median wavelengths corresponding to the PL bandgap, the peak in the LSW PL spectrum and the Fermi level. d) Threshold carrier density vs QW ZSE width for 4374 NWs. The plot also includes the median carrier lifetimes and σ (disorder) values from the PL fitting (see Section 4). e) Threshold carrier density vs NW length for 2099 NWs, a linear fit through the data is shown as a guide to the eye. f) Threshold carrier density vs carrier lifetime for 2061 NWs, a linear fit through the data is shown as a guide to the eye.

with a lower density of defects, results in a lower threshold. By improving the gain medium quality, by, for example, optimising the growth of the unintentionally defective NW tip,[32] the threshold can be minimised.

σ is a measure of the disorder in the QWs, which is extracted from the FWHM of the PL spectra. As shown in Figure 4b, the median value of σ varies between 16 meV and 13 meV and is strongly negatively correlated with the the carrier lifetime. This correlation is statistically significant, with a Pearson's r value of -0.18 and a p-value close to zero. Therefore, a NW with a lower defect density also has a smaller σ, and a reduced degree of disorder. This correlation is expected since defects and optoelectronic disorder typically go hand-in-hand. Table 1 demonstrates that this results in a statistically significant negative correlation between σ and the lasing threshold. This trend is compatible by the variation in the power factor, extracted from the stretched exponential fitting of the PL decays, which is smaller for larger values of sigma, and higher thresholds (Figure 4b). A smaller power factor is the result of a greater deviation from an exponential PL decays, which is another signature of disorder within the system.[28] More statistics on the power factor can be found in the Supporting Information.

Intriguingly Table 1 also shows that there is no significant correlation between the ZSE width of the thicker QW-shell and the lasing performance. In contrast, changes in the ZSE width of the thinner QW-core cause changes in all of the performance metrics. This means that it is solely QW-core that is the gain medium in this laser system. This is an important observation that is facilitated by the high-throughput approach and can be used to inform future NWL production by removing the QWs that do not contribute to the gain.

There is a positive correlation between the QW-core ZSE width and lasing wavelength: this is shown in Figure 4c, and corresponds to a redshift of the median lasing wavelength of approximately 20 nm for an increase in the QW-core ZSE width from 3.5 nm to 3.9 nm. As shown in Figure 4c, we would only expect a redshift of 13 nm in the bandgap over this range due to a reduction in the quantum confinement energy. The observed variation is therefore is a steeper than the trend in the PL bandgap, and it can not be explained purely by a reduction in the quantum confinement energy.

To explain this additional wavelength shift, we initially consider an increase in the bandfilling effects for narrower QW-cores, due to a reduced number of states. As shown in Figure 4c, the median PL peak shifts by approximately 15 nm across the dataset. Therefore, there is an additional 5 nm redshift that is unaccounted for. We tentatively assign this to a shift in the lasing gain curve due to changes in the mode overlap

with the QW-core as the lasing wavelength and QW-core ZSE width change. It is difficult to analytically quantify this effect at this stage, but this observation offers an interesting direction for future studies.

The QW-core ZSE width also has a negative correlation with the lasing threshold, as shown in Figure 4d. The median threshold carrier density decreases from 6.3×10^{15} cm^{-2} to 4.3×10^{15} cm^{-2} for an increase in the QW ZSE width from 3.5 nm to 3.95 nm. This variation can largely be explained by considering how the QW ZSE width is coupled to the QW properties, which is demonstrated in Figure 4d. A narrower QW-core results in increased values of σ, and therefore increased disorder, which is compatible with previous studies.[34] These narrower QW-cores also have, on average, a faster recombination lifetime: this suggests that there may be a faster non-radiative recombination rate and thus a higher density of defects. The nature of these defects is currently unknown, and is a topic for further study: however, they are not likely to be strain related, as a previous study found no evidence of misfit dislocations at the GaAsP/GaAs interfaces. Despite this uncertainty over the type of defects, it is clear that the quality of the QW-cores can be improved by targeting a wider QW-core during growth, which will lead to lower thresholds.

The effect of the lasing cavity on the performance can be gauged by studying the impact of the NW dimensions. Table 1 demonstrates that the NW width has no statistically significant impact on performance. This is likely to occur for NWLs that are wide in comparison to the lasing wavelength, and has been theoretically predicted for both AlGaAs/GaAs [15] and InP [26] NWLs. The NWs in this study have a mean width of $(0.77 \pm 0.25)\mu$m, which is significantly larger than the lasing modal wavelength, $\lambda/n = 270$ nm. Furthermore, as the lasing gain originates solely from the QW closest to the NW core, it is reasonable to expect strong confinement of the mode to the lasing cavity and furthermore that the modal refractive index is not significantly affected by the NW width. This conclusion is also consistent with analysis in the Supporting Information that shows a small uncertainty in the refractive index that does not correlate with NW width.

The NW length also has no impact upon the lasing wavelength, likely because these are an order of magnitude longer than the lasing wavelengths, so any impact of longitudinal mode selection will be minimal. Table 1 shows that there is a slight negative correlation with the threshold, which is shown in Figure 4e. A similar trend has been observed previously in AlGaAs/GaAs MQW NWLs,[19] which was attributed to gain in the cavity overcoming the end-facet losses with increasing length. Whilst this is expected for the GaAsP/GaAs NWLs, Table 1 shows that changes in the distributed losses, α, do not correlate with the performance, and so this effect will be small with respect to the other observed trends. For these wires, a larger effect is an observed correlation between the NW length and the carrier lifetime, as shown in Figure 4f: this means that a longer NW will, on average, have a longer carrier recombination time, a higher quality QW and therefore a lower threshold. This is compatible with a previous transmission electron microscopy study on these NWs that observed the formation of a high density of threading dislocations close to the NW tip.[32] These dislocations act as non-radiative recombination centres, but as the nominal NW length increases, the relative importance of this recombination pathway will be reduced because the proportion of the gain medium that is defective will be lower. This, in turn, results in a lower threshold.

The cavity reflectivity does not correlate with the wavelength or threshold. Additionally, there is no relationship between the cavity reflectivity and the NW width: this is consistent with the large NW widths and the lack of correlation between NW width and performance.

However, the result for α is surprising, which is expected to impact the lasing performance.[35] However, this result does not preclude the effect α on performance, merely that variation in the gain medium (i.e., carrier lifetime and QW width) has a stronger and limiting impact on the performance. Due to the large number of independent variables and complex inter-dependencies in this data, these conclusions can only be reached through the big-data approach.

3. Conclusion

A multi-modal automated optical characterization approach was developed to study the performance of a large number of individual NW lasers, including optical imaging, spectroscopic, single-photon counting and interferometric measurements. When applied to 5195 GaAsP/GaAs NW lasers, this created a multi-dimensional dataset including 18320 individual measurements. Correlations were drawn between structural (e.g. length, width) , material (e.g. bandgap, carrier), cavity (e.g. reflectivity, losses) and functional (e.g. lasing threshold, wavelength) properties to gain a deeper understanding into the processes that govern lasing performance and establish the route to improve this performance.

By analysing the PL lineshape, it was found that the properties of only the QW closest to the NW core correlated with the lasing performance. This both enabled the unambiguous identification of the gain medium, and provided the means to calculate the carrier density in the QW at threshold.

The performance metrics of threshold carrier density and lasing wavelength were compared with independent measurements of the cavity and gain medium using a multiple linear regression model. This analysis demonstrated that the lasing wavelength was influenced by the lasing threshold, due to bandfilling effects and the QW width, partially due to quantum confinement effects. The width of the QWs also directly influences the disorder and the nonradiative defect density which leads to reduced thresholds for the wider QWs. The dominant factor influencing the lasing threshold was the carrier recombination lifetime. Therefore, to minimise the lasing threshold, further optimisation of the QW is required to minimise the non-radiative recombination rate, which can be achieved by increasing the length of the NWs and the width of the QWs.

This big-data approach to experimental analysis of NWLs can therefore provide conclusions that are not accessible using small-population studies. Crucially, the approach needs minimal a priori information, in this case only requiring knowledge of the refractive index and the core/shell heterostructure and can be widely applied to similar materials systems.

4. Experimental Section

Sample Growth: The NWs reported in this paper were grown to a previously published recipe using self-catalysed molecular beam epitaxy on Si substrates.[25] The NW core has a nominal width of 80 nm and a composition of $GaAs_{0.38}P_{0.62}$. This is followed by three GaAs QWs with 40 nm $GaAs_{0.47}P_{0.53}$ barriers and a 30 nm $Al_{0.5}Ga_{0.5}As_{0.53}P_{0.47}$ passivation layer.

Before characterisation, the NWs from these arrays were transferred onto a Si substrate via ultrasonication and drop casting.[31] The result was a large population of NWs (>5000) in the plane of the substrate, which is ideal for detailed optical characterisation.

Automated Microscopy: To characterise the geometry and the optoelectronic performance of the NWs, the transferred substrate was placed in a bespoke, automated optical microscope. This setup utilised a 20x objective lens with a numerical aperture of 0.75 and a working distance of 1 mm. The objective was vertically mounted on a P.I. V-308 translation stage. Optical imaging was performed using front illumination with a 200 mm focal length tube lens to produce a magnified image with a spatial resolution of 1 µm. Confocal laser excitation was also possible using a series of beamsplitters.

The NW samples were placed on a P.I. V-738 x-y translation stage, capable of a travel range of 150 mm by 150 mm, with 0.1 µm precision. Initially, a pulse train from an excitation laser was focused onto the substrate to ablate material in order to create markers. These markers were separated by 2 mm and defined an x-y co-ordinate system on the substrate which could be used to uniquely locate each object.

The NWs were located using an automated microscopy procedure. This involved translating the x-y stage to a new region of the substrate, refocusing the objective lens to correct for any slope in the sample and imaging the surface. A machine vision algorithm automatically identified NWs based on their dimensions and appearance. The location, width, length and orientation angle for each NW was recorded, along with the optical image. This was repeated, moving to a different location on the substrate to identify more wires. The procedure is entirely scaleable, and can be left to run until a suitable NW population is identified, which was 5195 NWs in this study. Each identified NW was then investigated using different experimental modules (spectroscopy and imaging, TCSPC, interferometry and distributed losses), which are discussed in separate sections below.

Scanning Electron Microscopy: SEM measurements were performed on the transferred NWs using the secondary electron detector of a Quanta250 field emission gun microscope, with an acceleration voltage of 15 keV and a magnification of 522x. A series of SEM images were measured across a 2 mm by 2 mm square on the transferred NW substrate: each image had a field of view of 290 µm by 250 µm, with a total of 90 images captured.

As the positions of each of the NWs identified in the optical microscopy are defined relative to a series of unique markers, the location (to within ≈5 µm) of each NW was identified by a transformation (translational and rotational) between the coordinate axes of the optical and SEM images. The machine vision algorithm was applied to identify the same NW in each dataset by identifying the geometrical features. This process enabled the width of the NWs to be determined, beyond the resolution limit of the optical microscopy, whilst permitting the removal of NWs from the analysis that were too close to be observed in the optical. Good registration was achieved for 2492 NWs. More details on the comparison between optical and SEM imaging are given in the SI.

Spectroscopy and Imaging Measurements: Automated PL measurements were performed on single NWs using a quasi-confocal arrangement in the optical microscope. For spectroscopy, the light emitted from an approximately 2 µm diameter spot was collected using an optical fibre. This was connected to a Horiba iHR550 spectrometer to measure the emission spectrum with a resolution of 1 nm. Emission imaging experiments were performed simultaneously by placing a suitable long-pass filter in front of the camera to remove the excitation.

Lasing experiments used the output from a PHAROS-ORPHEUS 200 fs optical parametric amplifier, at a wavelength of 633 nm, as the excitation source, using a band pass filter to clean-up the excitation spectrum. A uniform excitation spot was achieved using a telescopic beam expander and iris, along with a defocusing lens. The result was a top hat excitation spot with a diameter of 73 µm, capable of achieving excitation fluences up to 2000 µJ cm^{-2}. This experiment was performed successfully on 4374 NWs.

PL spectra were fit with a modified LSW model, that has been adapted from refs. [22,29] and is given in terms of the photon energy E by Eq. 3:

$$I_{LSW}(E) = CE^2 \frac{W(E)}{\exp\frac{E-(E_F+E_g)}{k_BT}-1} \tag{3}$$

where C is an amplitude term, E_F is the quasi-fermi energy, E_g is the energy bandgap of the QW (accounting for confinement energy), T is the carrier temperature and k_B is the Boltzmann constant. $W(E)$ describes the absorption of the NW, which can be approximated using Eq. 4,[36,37]

$$W(E) = (1-\exp(B(E)))\left(1-\frac{2}{\left(\exp\frac{E-(E_F+E_g)}{k_BT}\right)^{1/2}+1}\right) \tag{4}$$

where $B(E)$ is the 2D density of states of the QW. Due to disorder in the NW lattice on the nanoscale, the absorption and emission can extend into the expected bandgap with an Urbach tail.[38] To approximate this the model was modified to exponentially decay below the bandgap. Additionally, the spectrum was convoluted with a Gaussian function, G, with standard deviation σ, which is used to approximate micro-scale symmetrical inhomogeneity in the NW. The resulting fit is described by:

$$I_{PL}(E) = G(E) \otimes \begin{cases} I_{LSW}(E), & \text{if } E > E_g - dE \\ A\exp\left(\frac{E-E_g}{E_U}\right), & \text{if } E < E_g - dE \end{cases} \tag{5}$$

where E_U is the Urbach energy, A is an amplitude term and dE is a small offset energy required to connect the two energy regimes.

The excitation fluence dependent measurements were performed using an automated neutral density filter wheel to change the degree of attenuation of the excitation beam: this provided up to 47 emission spectra per NW, showing both PL and lasing peaks when above the threshold fluence, as demonstrated in Figure 2a. From this data, the threshold fluence was obtained by extrapolating the trend of the lasing peak intensity with fluence. The performance did not depend upon the orientation of the NWs. An example of this analysis is provided in the Supporting Information.

Additionally, the variation of the PL with fluence was extracted by using a median filter to remove the lasing peaks. A global fit of the LSW model was applied to all of the PL spectra, keeping the optical bandgap, inhomogeneous broadening, carrier temperature and Urbach energy constant. This approach determined the quasi-fermi energy, E_F, in each QW, as shown in Figure 2b. Importantly, this fit requires two optically active QWs to recover the shape of the emission spectrum of a single NW. To simplify the analysis, the thickness of one of these QWs was fixed to the value obtained in the low fluence PL fitting. Additionally, the E_F in each QW was assumed to be related by a constant. This approach was used to calculate the time-averaged carrier density at every fluence studied, for each optically active QW, $\langle n_{QW} \rangle$, using the 2D density of states, yielding:

$$\langle n_{QW} \rangle = \frac{\mu E_F}{\pi \hbar^2} \tag{6}$$

where µ is the reduced mass of an electron-hole pair. An example of this calculation is given in Figure 2b. Analysis of the change in PL intensity with excitation fluence also provides information regarding the

carrier recombination mechanisms. This data is discussed further in the Supporting Information.

Time-Correlated Single Photon Counting: The carrier recombination dynamics were measured by routing the optical fibre to a Picoharp HydraHarp400 TCSPC system with Silicon Single Photon Avalanche Photodiodes (SPADs) to measure the PL time decays with a 70 ps timing resolution. The PHAROS-ORPHEUS excitation source was used for these experiments with an excitation fluence of approximately 15 μJ cm^{-2}, below the lasing threshold of any of the NWLs. This was performed successfully on 5195 NWs. The experiment was then repeated at 60% of the threshold fluence.

An example of the PL decays at low power is shown in Figure 1c. As shown in the Supporting Information. The decay shapes are the result of both radiative and non-radiative decay paths and are well described by a stretched exponential fit, which was used to extract a representative lifetime, τ, given by,

$$I = I_0 \exp - \left(\frac{t}{\tau}\right)^{\beta} \tag{7}$$

where β is a factor describing the degree of exponentiality, which is an additional measure of disorder in the NWs. β has a median value and SD of (0.74 ± 0.09), and correlates with other measures of disorder, such as σ. More statistics on β are provided in the Supporting Information.

The decays close to threshold were used, along with $\langle n_{QW} \rangle$, to estimate the initial carrier density in the QWs, $n_{0,\,QW}$, at threshold. This was achieved by averaging the area under the PL decay curve, $f(t)$, over the time period of the laser repetition rate (5 μs), using:

$$n_{0,QW} = \frac{5\,\mu s \times \langle n_{QW} \rangle}{\int_0^{5\,\mu s} f(t)\,dt} \tag{8}$$

This approach enabled the calculation of the threshold carrier density—which is a more direct measurement of the lasing threshold than the threshold fluence, as it decouples the lasing mechanism from complicated effects such as light absorption in the NW and carrier capture in the QWs. The Supporting Information contains more details regarding the PL decays close to threshold, along with a comparison between the threshold fluence and threshold carrier densities.

Interferometric Measurements of Cavity Reflectivity: To measure the reflectivity of the NW laser cavity, the NWs were excited with a fluence above the lasing threshold. The emission from the NW end-facets was analysed by a time-gated Michelson interferometer that has been previously discussed.[24] For each NW, one of the interferometric mirrors was automatically translated through the zero path length position, using SPADs to detect the interference fringes, such as those inset in Figure 2c. To accelerate the experiment, the interference fringes were sampled at different positions along the path. These measurements were successfully performed for 724 NWs.

The interferograms for each NW were automatically processed using a Fourier filter to extract the interference fringes associated with frequencies close to the lasing wavelength. A peak detection algorithm was applied to calculate the fringe visibility, V, from the peak intensities I, at different distances, defined by:

$$V = \frac{I_{max} - I_{min}}{I_{max} + I_{min}} \tag{9}$$

An example of the fringe visibilities are shown in Figure 2c. The coherence length, L_{coh} of the lasing light was extracted from a FWHM of a Gaussian fit to the data. This value was then used to calculate the cavity reflectivity, R, using:

$$R = \exp\left(\frac{-2\pi n L}{L_{coh}}\right) \tag{10}$$

where L is the NW length, extracted from the microscopy. n is the modal refractive index of the wire. As the NW widths are large, and the lasing modes are well confined to the NW, we approximate this to be equal to the bulk value of 3.4.[39] The refractive index also varies slightly between different NWs: by analysing the longitudinal mode spacing, the upper limit of the uncertainty on this parameter was estimated to be +/−0.5, or a percentage uncertainty of 15% (more information can be found in the Supporting Information). R is the geometric mean of the reflectivity of both NW end-facets. The reflectivity of each end-facet was extracted using complementary imaging, which is discussed in the Supporting Information.

Distributed Losses: The distributed losses were measured by exciting the NWs using a 2 μm-diameter focused spot from a low-power continuous wave HeNe laser, and examining the spatial distribution of the low fluence emission using the imaging camera. The diffusion length in the NWs is expected to be sub-μm, and so carriers recombine close to where they are generated. As shown in Figure 2d, this results in a bright emission from the NWs that is co-incident with the excitation spot. However, a portion of the emitted light is confined to the NW due to waveguiding effects: this light travels along the wire and couples out of the end-facets, which is seen in the image.

To quantify the attenuation of the light as it travels down the wire, the automated microscopy approach was used to find the lengths and in-plane orientation angles of each nanowire: the excitation spot position was then automatically scanned along the length of the wire, and the intensity of light coupling from each facet was monitored by recording a series of images. This approach is similar to that employed in ref. [23], and was applied to 267 NWs, an example is shown in Figure 2d.

This data was fit using Equation (2), where the intensity ratio is studied to minimize the impact of changes in the coupling of the excitation into the NW due to slight misalignment during the scan.

Supporting Information

Supporting Information is available from the Wiley Online Library or from the author.

Acknowledgements

This was work funded by UKRI under grant MR/T021519/1 and EP/V036343/1.

Conflict of Interest

The authors declare no conflict of interest.

Author Contributions

Stephen Church: formal analysis, investigation, methodology, software, visualisation, writing - original draft. Nikesh Patel: formal analysis, investigation, writing - review and editing. Ruqaiya Al-Abri: investigation, writing - review and editing. Nawal Al-Amairi: formal analysis, writing - review and editing. Yunyan Zhang: resources, writing - review and editing. Huiyun Liu: resources, writing - review and editing. Patrick Parkinson: conceptualization, data curation, funding acquisition, methodology, software, supervision, writing - review and editing.

Data Availability Statement

The data that support the findings of this study are openly available in figshare at https://doi.org/10.48420/21865785. The code to perform the

analysis is available in figshare at https://doi.org/10.48420/21865545 and on github at https://github.com/p-parkinson.

Keywords

high-throughput, interferometry, nanowire lasers, photoluminescence

Received: October 19, 2022
Revised: December 15, 2022
Published online:

[1] A. V. Maslov, C. Z. Ning, *Appl. Phys. Lett.* **2003**, *83*, 1237.
[2] D. Jevtics, A. Hurtado, B. Guilhabert, J. McPhillimy, G. Cantarella, Q. Gao, H. H. Tan, C. Jagadish, M. J. Strain, M. D. Dawson, *Nano Lett.* **2017**, *17*, 5990.
[3] X. Wu, Q. Chen, P. Xu, Y.-C. Chen, B. Wu, R. M. Coleman, L. Tong, X. Fan, *Nanoscale* **2018**, *10*, 9729.
[4] B. Mayer, L. Janker, B. Loitsch, J. Treu, T. Kostenbader, S. Lichtmannecker, T. Reichert, S. Morkötter, M. Kaniber, G. Abstreiter, C. Gies, G. Koblmüller, J. J. Finley, *Nano Lett.* **2016**, *16*, 152.
[5] E. Bermúdez-Ureña, G. Tutuncuoglu, J. Cuerda, C. L. C. Smith, J. Bravo-Abad, S. I. Bozhevolnyi, A. Fontcuberta i Morral, F. J. García-Vidal, R. Quidant, *Nano Lett.* **2017**, *17*, 747.
[6] J. C. Johnson, H. Yan, P. Yang, R. J. Saykally, *J. Phys. Chem. B* **2003**, *107*, 8816.
[7] J. C. Johnson, H.-J. Choi, K. P. Knutsen, R. D. Schaller, P. Yang, R. J. Saykally, *Nat. Mater.* **2002**, *1*, 106.
[8] S. Gradečak, F. Qian, Y. Li, H.-G. Park, C. M. Lieber, *Appl. Phys. Lett.* **2005**, *87*, 173111.
[9] X. Duan, Y. Huang, R. Agarwal, C. M. C. Lieber, C. G. Fast, *Nature* **2003**, *421*, 241.
[10] X. Wang, M. Shoaib, X. Wang, X. Zhang, M. He, Z. Luo, W. Zheng, H. Li, T. Yang, X. Zhu, L. Ma, A. Pan, *ACS Nano* **2018**, *12*, 6170.
[11] D. Saxena, S. Mokkapati, P. Parkinson, N. Jiang, Q. Gao, H. H. Tan, C. Jagadish, *Nat. Photonics* **2013**, *7*, 963.
[12] Q. Gao, D. Saxena, F. Wang, L. Fu, S. Mokkapati, Y. Guo, L. Li, J. Wong-Leung, P. Caroff, H. H. Tan, C. Jagadish, *Nano Lett.* **2014**, *14*, 5206.
[13] Y. Xiao, C. Meng, P. Wang, Y. Ye, H. Yu, S. Wang, F. Gu, L. Dai, L. Tong, *Nano Lett.* **2011**, *11*, 1122.
[14] F. Qian, Y. Li, S. Gradečak, H.-G. Park, Y. Dong, Y. Ding, Z. L. Wang, C. M. Lieber, *Nat. Mater.* **2008**, *7*, 701.
[15] D. Saxena, N. Jiang, X. Yuan, S. Mokkapati, Y. Guo, H. H. Tan, C. Jagadish, *Nano Lett.* **2016**, *16*, 5080.
[16] S. A. Church, R. Al-Abri, P. Parkinson, D. Saxena, *Prog. Quantum Electron.* **2022**, 100408.
[17] G. Aman, F. Mohammadi, M. Fränzl, M. Lysevych, H. H. Tan, C. Jagadish, H. Schmitzer, M. Cahay, H. P. Wagner, *Sci. Rep.* **2021**, *11*, 21378.
[18] M. A. Zimmler, F. Capasso, S. Müller, C. Ronning, *Semicond. Sci. Technol.* **2010**, *25*, 024001.
[19] J. A. Alanis, D. Saxena, S. Mokkapati, N. Jiang, K. Peng, X. Tang, L. Fu, H. H. Tan, C. Jagadish, P. Parkinson, *Nano Lett.* **2017**, *17*, 4860.
[20] X. Zhang, H. Yang, Y. Zhang, H. Liu, *Nanotechnology* **2021**, *33*, 035202.
[21] R. Al-Abri, H. Choi, P. Parkinson, *J. Phys. Photonics* **2021**, *3*, 022004.
[22] S. A. Church, H. Choi, N. Al-Amairi, R. Al-Abri, E. Sanders, E. Oksenberg, E. Joselevich, P. W. Parkinson, *ACS Nano* **2022**, *16*, 9086.
[23] C. J. Barrelet, A. B. Greytak, C. M. Lieber, *Nano Lett.* **2004**, *4*, 1981.
[24] S. Skalsky, Y. Zhang, J. A. Alanis, H. A. Fonseka, A. M. Sanchez, H. Liu, P. Parkinson, *Light Sci. Appl.* **2020**, *9*, 43.
[25] Y. Zhang, G. Davis, H. A. Fonseka, A. Velichko, A. Gustafsson, T. Godde, D. Saxena, M. Aagesen, P. W. Parkinson, J. A. Gott, S. Huo, A. M. Sanchez, D. J. Mowbray, H. Liu, *ACS Nano* **2019**, *13*, 5931.
[26] D. Saxena, F. Wang, Q. Gao, S. Mokkapati, H. H. Tan, C. Jagadish, *Nano Lett.* **2015**, *15*, 5342.
[27] J. A. Alanis, M. Lysevych, T. Burgess, D. Saxena, S. Mokkapati, S. Skalsky, X. Tang, P. Mitchell, A. S. Walton, H. H. Tan, C. Jagadish, P. Parkinson, *Nano Lett.* **2019**, *19*, 362.
[28] D. Dyer, S. A. Church, M. Jain, M. J. Kappers, M. Frentrup, D. J. Wallis, R. A. Oliver, D. J. Binks, *J. Appl. Phys.* **2021**, *130*, 085705.
[29] E. M. T. Fadaly, A. Dijkstra, J. R. Suckert, D. Ziss, M. A. J. van Tilburg, C. Mao, Y. Ren, V. T. van Lange, K. Korzun, S. Kölling, M. A. Verheijen, D. Busse, C. Rödl, J. Furthmüller, F. Bechstedt, J. Stangl, J. J. Finley, S. Botti, J. E. M. Haverkort, E. P. A. M. Bakkers, *Nature* **2020**, *580*, 205.
[30] H. Zhu, Y. Fu, F. Meng, X. Wu, Z. Gong, Q. Ding, M. V. Gustafsson, M. T. Trinh, S. Jin, X.-Y. Y. Zhu, *Nat. Mater.* **2015**, *14*, 636.
[31] J. A. Alanis, Q. Chen, M. Lysevych, T. Burgess, L. Li, Z. Liu, H. H. Tan, C. Jagadish, P. Parkinson, *Nanoscale Adv.* **2019**, *1*, 4393.
[32] Y. Zhang, G. Davis, H. A. Fonseka, A. Velichko, A. Gustafsson, T. Godde, D. Saxena, M. Aagesen, P. W. Parkinson, J. A. Gott, S. Huo, A. M. Sanchez, D. J. Mowbray, H. Liu, *ACS Nano* **2019**, *13*, 5931.
[33] M. Vening, D. J. Dunstan, K. P. Homewood, *Phys. Rev. B* **1993**, *48*, 2412.
[34] C. L. Davies, P. Parkinson, N. Jiang, J. L. Boland, S. Conesa-Boj, H. Hoe Tan, C. Jagadish, L. M. Herz, M. B. Johnston, *Nanoscale* **2015**, *7*, 20531.
[35] S. Hirano, N. Takeuchi, S. Shimada, K. Masuya, K. Ibe, H. Tsunakawa, M. Kuwabara, *Jpn. J. Appl. Phys.* **2005**, *98*, 094305.
[36] G. Lasher, F. Stern, *Phys. Rev.* **1964**, *133*, A553.
[37] P. Wurfel, *J. Phys. C: Solid State Phys.* **1982**, *15*, 3967.
[38] Y. Natsume, H. Sakata, T. Hirayama, *Phys. Status Solidi A* **1995**, *148*, 485.
[39] S. Adachi, *Jpn. J. Appl. Phys.* **1989**, *66*, 6030.